applied sciences

MDPI

Article

Lossless Compression of Large Aperture Static Imaging Spectrometer Data †

Lu Yu [1,*], Hongbo Li [2], Jing Li [1] and Wei Li [1]

[1] Department of Information Science, Xi'an University of Technology, Xi'an 710048, China
[2] Key Laboratory of Spectral Imaging Technology CAS, Xi'an Institute of Optics and Precision Mechanics of CAS, Xi'an 710119, China
* Correspondence: yulu@xaut.edu.cn

† This paper is an extended version of our paper published in MIPPR2017.

Abstract: The large-aperture static imaging spectrometer (LASIS) is an interference spectrometer with high device stability, high throughput, a wide spectral range, and a high spectral resolution. One frame image of the original data cube acquired by the LASIS shows the image superimposed with interference fringes, which is distinctly different from traditional hyperspectral images. For compression studies using this new type of data, a lossless compression scheme that combines a novel data rearrange method and the lossless multispectral and hyperspectral image compression standard CCSDS-123 is presented. In the rearrange approach, the LASIS data cube is rearranged such that the interference information overlapped on the image can be separated, and the results are then processed using the CCSDS-123 standard. Then, several experiments are conducted to investigate the performance of the rearrange method and examine the impact of different CCSDS-123 parameter settings for the LASIS. The experimental results indicate that the proposed scheme provides a 32.9% higher ratio than traditional rearrange methods. Moreover, an adequate parameter combination for this compression scheme for LASIS is presented, and it yields a 19.6% improvement over the default settings suggested by the standard.

Keywords: LASIS; optical image processing; interference spectrometer; lossless compression

Citation: Yu, L.; Li, H.; Li, J.; Li, W. Lossless Compression of Large Aperture Static Imaging Spectrometer Data. *Appl. Sci.* **2023**, *13*, 5632. https://doi.org/10.3390/app13095632

Academic Editor: Andrés Márquez

Received: 27 March 2023
Revised: 29 April 2023
Accepted: 30 April 2023
Published: 3 May 2023

1. Introduction

Ongoing interest within the realm of remote sensing applications has led to the dramatic development of hyperspectral sensors, which possess high spatial and spectral resolution, having hundreds or thousands of bands. In particular, the stationary imaging Fourier transform spectrometer (SIFTS) has been given considerable attention because it does not employ any moving parts [1], and much effort has been invested in its development for use in airborne and spaceborne missions, such as the spatially modulated imaging Fourier transform spectrometer (SMIFTS), the Fourier transform visible hyperspectral imager (FTVHSI), the Fourier transform hyperspectral imager (FTHSI), the digital array scanned interferometer (DASI), the high-efficiency hyperspectral imager (HEHSI), and the hyperspectral imaging system SYSIPHE [2]. However, traditional SIFTSs all have a slit that greatly reduces the utilization of energy [3]. The large aperture static imaging spectrometer (LASIS) is a temporally–spatially modulated imaging interferometer that was developed in the late 1990s [4,5]. Because the slit is eliminated in the optical system of the LASIS, it has a much higher throughput than conventional SIFTSs. Additionally, this system offers benefits such as a high luminous flux, spectral linearity, a lightweight structure, and a broad spectral range while effectively resolving the challenge of maintaining high optical flux and stability. In recent years, several interferometers that use LASIS-like principles have been proposed, such as the aerospace leap-frog imaging static interferometer for earth observation (ALISEO) [6], the long wavelength infrared (LWIR) hyperspectral imager [7], and the large-aperture spatial heterodyne imaging spectrometer (LASHIS) [8–10].

As is well known, the hyperspectral imager obtains a large volume of three-dimensional data cubes consisting of one spectral and two spatial dimensions, and the transmission and storage of the huge amounts of data present special challenges. Therefore, efficient compression techniques are required to resolve this problem. Considerable research has been conducted in the area of hyperspectral data compression [11–16]. Nevertheless, LASIS data and traditional hyperspectral data exhibit distinct discrepancies. A frame of LASIS data contains spatial information in one spatial direction, and interference information is superimposed on spatial information in the other spatial direction, which is also the optical path difference (OPD) direction. Each row of the 2D detector array corresponds with a different OPD band. Each column of the array samples a different spatial location, and the array, therefore, has a spatial-OPD layout. However, the unique characteristics of LASIS data introduce new problems for data compression.

Because of the practical applications of LASIS data in engineering, studies have been conducted to identify compression methods for this new type of data. Deng [17] proposed a compression technique that utilizes the rectangle region of interest (ROI) coding from EBCOT, which does not lift the coefficients of the wavelet domain and is complemented by adaptively computing the distortion in the code stream organization. Xiao [18] employed a matching algorithm in the wavelet domain to reduce the redundancy in two successive LASIS frames and then applied a new ROI coding algorithm in the code stream organization stage to substitute the DWT suggested by JPEG2000. Ma [19] improved the weighted rate–distortion optimization for SPIHT after analyzing the correlation between the distortion in the Fourier domain and compression in the spatial domain. To improve the performance of this method, Wang [20] applied the partial SPIHT with classified weighted rate–distortion optimization. Li [21] introduced a wavelet transform based on three-dimensional orientation prediction in the compression approach of LASIS. However, the unique features of LASIS have not been fully explored. LASIS data are usually processed directly as traditional hyperspectral data or rearranged into an interferogram cube called LAMIS [19,20] in these approaches. In addition, most of the approaches exploit spectral redundancy as well as the spatial dimension and have been lossy compression algorithms [22]. Although these algorithms lead to a much higher compression ratio, information is discarded in the process. In most of the corresponding applications of LASIS, the information loss resulting from the use of lossy compression algorithms is unacceptable. Hence, lossless compression algorithms are needed for this new type of data to avoid useful information retrieval degradation.

In this paper, we focus on the lossless compression of LASIS data. Taking into consideration the unique characteristics of LASIS, we have divided the lossless compression process of LASIS images into three components: data rearrangement, prediction, and coding. The novel stage, data rearrange, refers to selecting a permutation of the data cube in which the interference and spatial information along the columns can be separated. In this way, we can make better use of the correlation in the spatial and OPD dimensions. The Multispectral and Hyperspectral Data Compression (MHDC) working group of the Consultative Committee for Space Data Systems (CCSDS) has designed the standardized CCSDS-123, primarily for the onboard lossless compression of multispectral and hyperspectral images [23]. This standard is then employed in the two later stages because it has a combination of low computational complexity and compression effectiveness. The standard includes several user-specified configuration parameters, and previous work has allowed users to determine suitable values for these parameters for a variety of sensors [12,24,25]. However, relevant studies on LASIS have not been performed. Finally, a series of experiments are conducted to evaluate the efficiency of the proposed compression scheme on real LASIS data and optimize the compression settings involved. These experimental results can offer instructive guidance regarding lossless compression in other hyperspectral interferometers based on LASIS-like principles.

The subsequent sections of this paper are organized as follows: Section 2 presents an overview of the imaging principle and the unique data characteristics of the LASIS sensor.

Section 3 details the proposed compression scheme. Section 4 presents the experimental results of the proposed techniques conducted on real LASIS data. Section 5 provides some conclusions and summarizes the paper.

2. Instrument and Data Characteristics

Conventional hyperspectral imagers, both interference and dispersive spectrometers, are all equipped with a slit that greatly decreases energy utilization. By adding a lateral shearing interferometer to a conventional imaging system, the energy utilization ratio of the LASIS is nearly equivalent to that of ordinary cameras and almost a hundred times greater than that of traditional hyperspectral imagers [8]. The imaging principle of LASIS is presented in Figure 1.

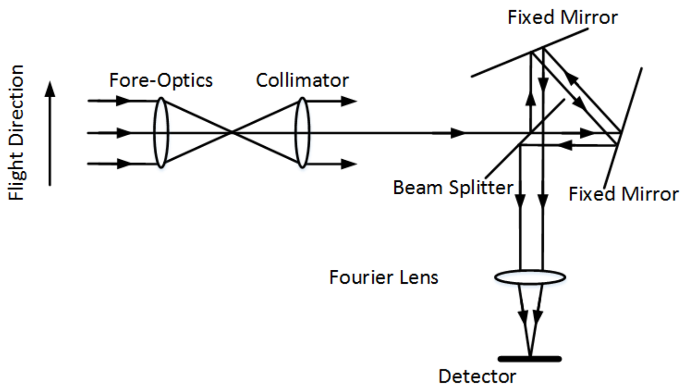

Figure 1. Image-forming principle of LASIS.

The original data collected by the LASIS instrument are called LASIS data. A frame of a LASIS cube, as depicted in Figure 2, is not a regular image, as it is a combination of both two-dimensional spatial information and interference fringes with uniform thickness. In the pushbroom scanning approach, each row of detectors continuously observes the same points in object space. Consequently, the interferogram of a spatial location can be extracted only after performing pushbroom scanning of the full field of view. The extracted interferogram data cube is defined as LAMIS, a frame of which contains one-dimensional spatial information and one-dimensional interference information. Figure 2 illustrates the interferogram and LAMIS data extraction process for the LASIS.

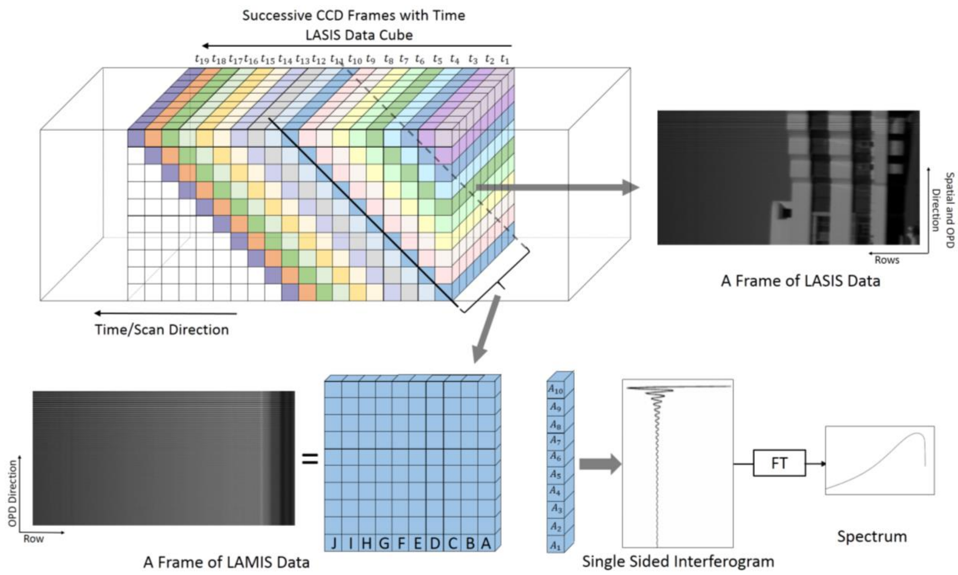

Figure 2. Interferogram and LAMIS data extraction process for the LASIS.

3. Compression Scheme

Due to the unique properties of the LASIS, we divide the lossless compression of LASIS images into three steps: data rearrangement, prediction, and encoding. The three functional stages of this compression scheme are provided in Figure 3.

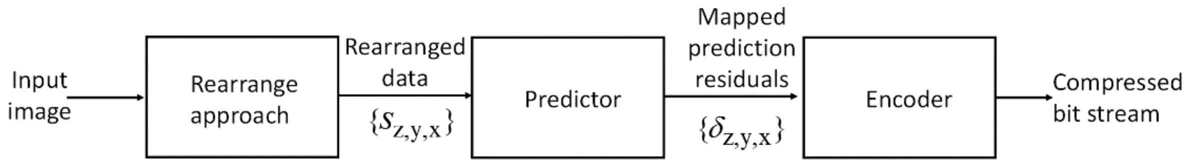

Figure 3. Compression scheme of the proposed method.

3.1. Data Rearrange

In the pushbroom scanning approach of the LASIS sensor, each row of the CCD detector successively observes the same points in object space. The regrouping of the same row of each frame of the LASIS data cube allows us to obtain a complete scene of the full field of view under the same optical path difference (OPD) as illustrated in Figure 4. By scanning through all the OPD positions, we can obtain a data cube that represents the response of the same field of view under all OPD bands. Since this data cube is similar to the form of data acquired by temporally modulated Fourier transform imaging spectrometers, i.e., dynamic interference imaging spectrometers, we denote this cube as a LADIS (Large-Aperture Dynamic Imaging Spectrometer). The extraction of the LADIS is a generalized coordinate transformation from the photo-acquisition space, $\phi_{(X,\ Y,\ F)}$, to the OPD-image space, $\phi_{(x,\ y,\ z)}$, as illustrated in Figure 5. The matrix formula for this generalized coordinate transformation can be written as

$$\begin{pmatrix} x \\ y \\ z - z_0 \end{pmatrix} = \begin{pmatrix} 1 & 0 & 0 \\ 0 & 1 & \frac{f}{H}\frac{v}{v_F} \\ 0 & \frac{f}{L} & 0 \end{pmatrix} \begin{pmatrix} X \\ Y \\ F \end{pmatrix}, \tag{1}$$

where f is the focal length of the Fourier lens; H is the height of the sensor; v is the relative velocity between the sensor and the ground; v_F is the frame frequency; L is the shear from the lateral shearing interferometer; F is the frame number in the photo-acquisition space, $\phi_{(X,Y,F)}$; z_0 is the zero OPD position in the OPD-image space, $\phi_{(x,y,z)}$; and z_0 can be assumed to correspond to $Y = 0$ in the photo-acquisition coordinate.

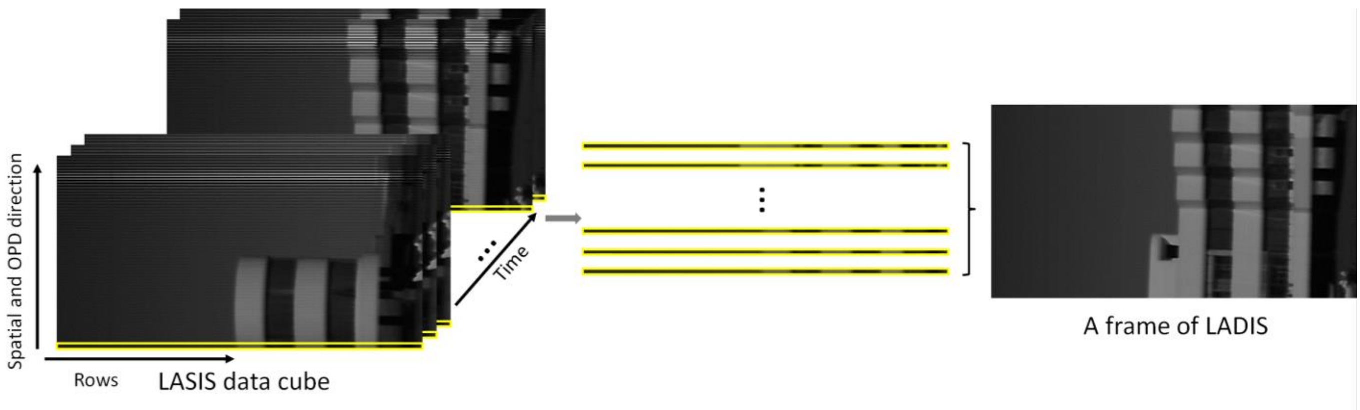

Figure 4. LADIS extraction procedure.

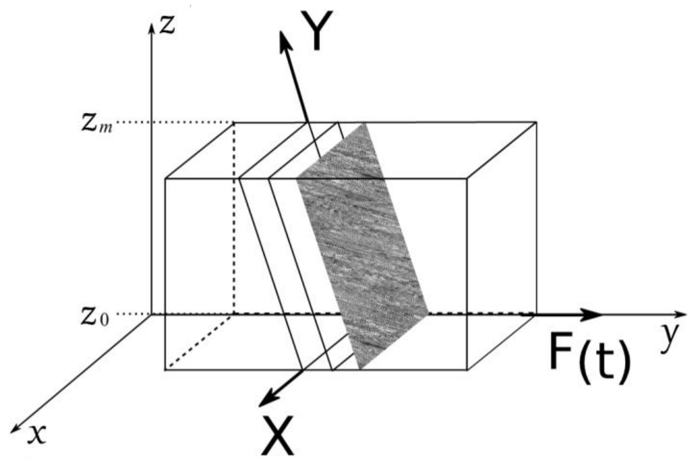

Figure 5. Photo-acquisition space, $\phi_{(X,Y,F)}$, and the OPD-image space, $\phi_{(x,y,z)}$.

Unlike the LASIS and LAMIS, a frame of LADIS data contains two-dimensional spatial information representing the response of all the pixels in the field of view under the same OPD. Therefore, the overlapped interference and spatial information in each frame can be separated. We can obtain the interferogram of a spatial location by extracting the same pixel of each frame.

3.2. The CCSDS-123 Standard

To facilitate an improved understanding of the experimental results, the CCSDS-123 algorithm is briefly described in this section.

3.2.1. Predictor

The predictor's task is to calculate the set of predicted sample values, $\{\hat{s}_{z,y,x}\}$, and mapped prediction residuals, $\{\delta_{z,y,x}\}$, from the input image samples, $\{s_{z,y,x}\}$, where x and y are the coordinates of the spatial dimensions, and the z index refers to the OPD band of the rearranged LADIS data. The prediction at sample $s_{z,y,x}$ is based on a set of previously sampled values, which include both the current band and P previous bands.

Two distinct prediction modes, namely, full and reduced, are offered by the standard. Each mode requires central local differences, $d_{z,y,x}$, from P previous bands, and the full mode additionally makes use of three directional local differences, $d^N_{z,y,x}$, $d^W_{z,y,x}$, and $d^{NW}_{z,y,x}$, in the current band. Figure 6 illustrates the two prediction modes, where only the differences depicted in blue are used in the calculation.

Local differences refer to the differences between the local sum values, $\sigma_{z,y,x}$, and the scaled values of the previous samples within the current band. In the case of the full prediction mode, the local differences vector, $\boldsymbol{U}_{z,y,x}$, is defined as

$$\boldsymbol{U}_{z,y,x} = \begin{bmatrix} d^N_{z,y,x} \\ d^W_{z,y,x} \\ d^{NW}_{z,y,x} \\ d_{z-1,y,x} \\ d_{z-2,y,x} \\ \vdots \\ d_{z-P^*_z,y,x} \end{bmatrix} = \begin{bmatrix} 4s_{z,y-1,x} - \sigma_{z,y,x} \\ 4s_{z,y,x-1} - \sigma_{z,y,x} \\ 4s_{z,y-1,x-1} - \sigma_{z,y,x} \\ 4s_{z-1,y,x} - \sigma_{z-1,y,x} \\ 4s_{z-2,y,x} - \sigma_{z-2,y,x} \\ \vdots \\ 4s_{z-P^*_z,y,x} - \sigma_{z-P^*_z,y,x} \end{bmatrix} \quad (2)$$

where $P^*_z = \min\{z, P\}$. Under the reduced mode, the first three components are not needed. There are two methods of calculating the local sum values, $\sigma_{z,y,x}$: neighbor-oriented and column-oriented.

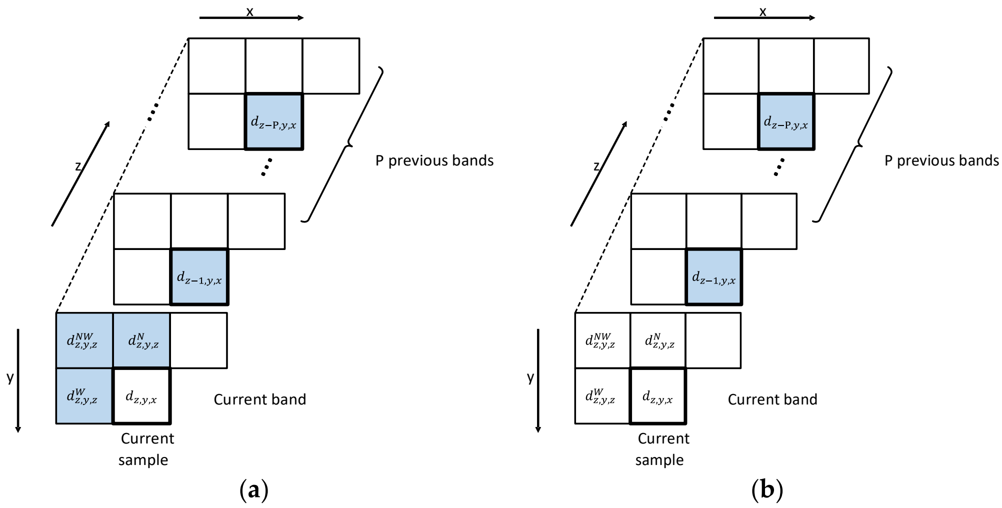

Figure 6. Local differences used under the full and reduced prediction modes: (**a**) full mode; (**b**) reduced mode.

The predicted central local difference, $\hat{d}_{z,y,x} = \boldsymbol{W}^T_{z,y,x}\boldsymbol{U}_{z,y,x}$, is a scaled prediction of $d_{z,y,x}$. The weight vector, $\boldsymbol{W}_{z,y,x}$, plays the role of measuring the contribution of each component of the local difference vector in the prediction procedure. The components of the weight vector are adaptively updated based on the sign of the prediction error, $e_{z,y,x} = 2s_{z,y,x} - \tilde{s}_{z,y,x}$. The value of the weight update scaling exponent, $\rho_{z,y,x}$, is determined by three user-specified parameters: the weight update scaling exponent initial parameter, ν_{min}; the weight update scaling exponent final parameter, ν_{max}; and the weight update scaling exponent change interval, t_{inc}. The rate at which the weights adapt to the image is impacted by $\rho_{z,y,x}$. A smaller value of $\rho_{z,y,x}$ results in faster adaptation but a worse steady-state performance. The resolution of the weight values is controlled by the weight component resolution parameter, Ω.

The main prediction calculation of the standard used to calculate the scaled prediction sample value, $\tilde{s}_{z,y,x}$, from the predicted central local difference, $\hat{d}_z(t)$, involves a parameter, R, to consider the register size. We can refer to the standard to obtain specific details. Reducing the register size increases the probability of overflow occurring in the calculation leading to a large prediction error. Although the compression will still be lossless, the compression effectiveness still suffers to an extent. Finally, to use the variable-length codes, the prediction residual, $\Delta_{z,y,x} = s_{z,y,x} - \left\lfloor \frac{\tilde{s}_{z,y,x}}{2} \right\rfloor$, is mapped to a nonnegative integer denoted as the mapped prediction residual, $\delta_{z,y,x}$, from which the decompressor can reconstruct the original sample value.

3.2.2. Encoder

A compressed image comprises two distinct parts: a header containing all compression settings and a body that consists of mapped prediction residuals that have been encoded losslessly. There are two different methods through which the mapped prediction residuals can be encoded: the sample-adaptive entropy coding approach and the block-adaptive approach.

The sample-adaptive entropy encoder utilizes a set of variable-length codes based on GPO2 codes to encode each mapped prediction residual, $\delta_{z,y,x}$. The initial state of the coder is determined by the initial count exponent, γ_0, and the accumulator initialization table, $\{k'_z\}_{z=0}^{N_z-1}$. The selection of the code is based on the ratio $\sum_{z,y,x} / \Gamma_{z,y,x}$; it is used to estimate of the average value of the mapped prediction residuals in each spectral band. The accumulator, $\sum_{z,y,x}$, and the counter, $\Gamma_{z,y,x}$, are adaptively updated, and the interval is determined by the rescaling counter size parameter, γ^*, during the encoding process. A smaller value of γ^* results in faster adaptation. The unary length limit parameter, U_{max}, is employed to constrain the length of the unary part of the codeword such that if the bit depth of the input image is D bits, then the maximum codeword length is $U_{\max} + D$ bits. In this way, the hardware implementation is simplified, and the cost of encoding poorly predicted samples is reduced.

Unlike the sample-adaptive approach, the block-adaptive entropy coder partitions the sequence of $\delta_{z,y,x}$ into blocks and selects an encoding method for each block. The components of each block are related to the sample encoding order. As a consequence, the encoding order and the block size have a substantial impact on the compression ratio under this approach.

4. Experimental Results

In order to validate the effectiveness of the proposed scheme, we conducted a series of experiments on 30 real data sets, including various scenes from Xi'an City and Yantai City, China, acquired by the LASIS equipment. The two-dimensional CCD detector is composed of 256 rows in the along-track direction that correspond to 256 OPD bands, as well as 500 columns in the cross-track direction, representing different spatial locations.

This section is divided into three parts to examine the influence of the three functional stages of the proposed compression approach on the overall compression performance. In each stage, several experiments are conducted for different related parameters, and one or more interrelated parameters are evaluated while the other parameters remain constant in each experiment. The compression performance is evaluated using the compression ratio, which is defined as the input image size divided by the compressed image size. A higher compression ratio implies better compression performance. The subsequent results display the average value obtained from all the test images.

4.1. Rearrange Method

The first experiment examines the impact of the data rearrange method introduced in Section 3.1 on the compression performance. The inter-frame correlation coefficients for the LASIS, LAMIS, and LADIS data cubes are calculated using Equation (3), where M is the number of rows, N is the number of columns in each frame, and $\bar{f}_i$ and $\bar{f}_j$ are the mean values of the i and j frames, respectively.

$$c_{i,j} = \frac{\sum_{x=1}^{M}\sum_{y=1}^{N}(f_i(x,y) - f_i) \times (f_j(x,y) - f_j)}{\sqrt{(\sum_{x=1}^{M}\sum_{y=1}^{N}(f_i(x,y) - f_i)^2)(\sum_{x=1}^{M}\sum_{y=1}^{N}(f_j(x,y) - f_j)^2)}} \quad (3)$$

Figure 7 depicts the correlation coefficients between each band of the LASIS, LAMIS, and LADIS and the average inter-frame correlation coefficient value computed except, for diagonal elements; the blue-to-red color map corresponds to the correlation coefficient values, ranging from 0 to 1. It can be seen that the correlation between each band of the LADIS is significantly higher than that of the LAMIS and LASIS, which will significantly improve the prediction accuracy, resulting in a much higher compression ratio, as shown in Figure 8. Under all four prediction mode and local sum type combinations of the CCSDS-123 standard, the rearranged LADIS data yield the best results by a considerable amount under all combinations compared with the LAMIS and LASIS data, and the original LASIS data produce the worst performance. The best performance of the proposed compression scheme is approximately 32.9% higher than that of the scheme that combines the traditional arrange approach with the standard. In the following experiments, we aim to optimize the relevant parameters of the proposed compression scheme.

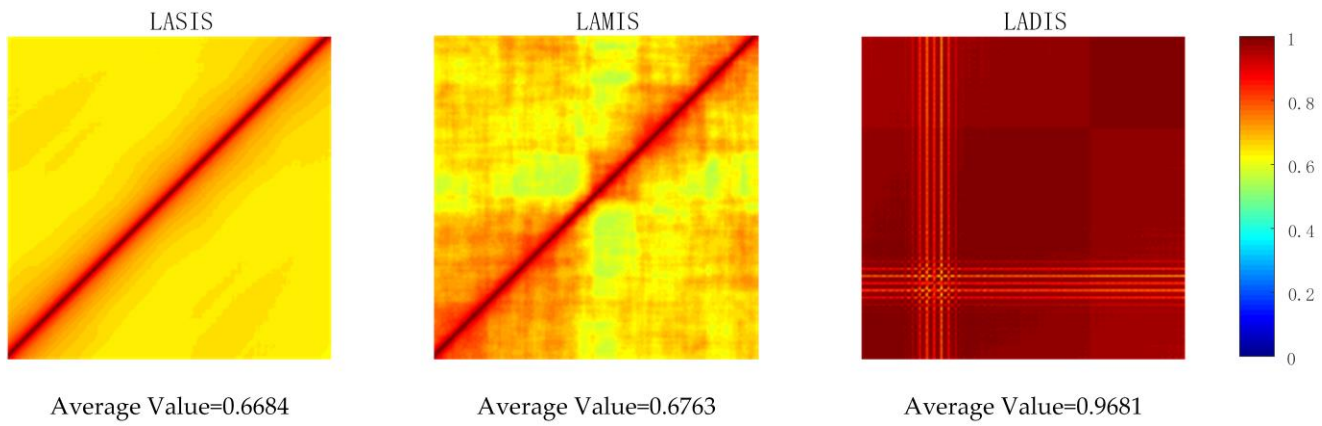

Figure 7. Correlation coefficients between each band of the LASIS, LAMIS, and LADIS.

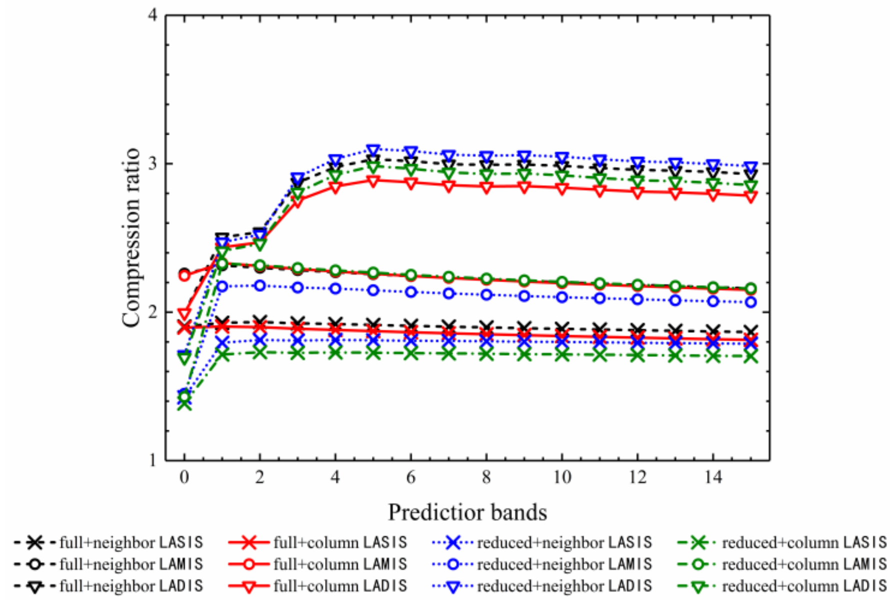

Figure 8. Compression ratio for different choices of rearrange methods under different prediction mode and local sum type combinations.

4.2. Predictor Settings

4.2.1. Prediction Mode, Local Sum Type, Number of Prediction Bands

Figure 9a illustrates the relationship between the compression ratio and the number of prediction bands, P, showcasing the effect of different options for the prediction mode and local sum type. The figure indicates that utilizing the reduced prediction mode in conjunction with the neighbor-oriented local sum type yields the best performance. Not using any prediction band (i.e., $P = 0$) results in the worst performance, as expected. The compression ratio increases along with the increment of P because the adjacent OPD bands have relatively few detail changes and strong inter-frame correlations, leading to good prediction performance. However, when the number of bands used for prediction reaches a certain value, the inter-band correlation decreases, and the improvement in prediction performance becomes less significant or even results in a decrease in prediction accuracy due to the marginal diminishing effect. We can see that the compression ratio curve tends to flatten or even decrease when the number of prediction bands is larger than five.

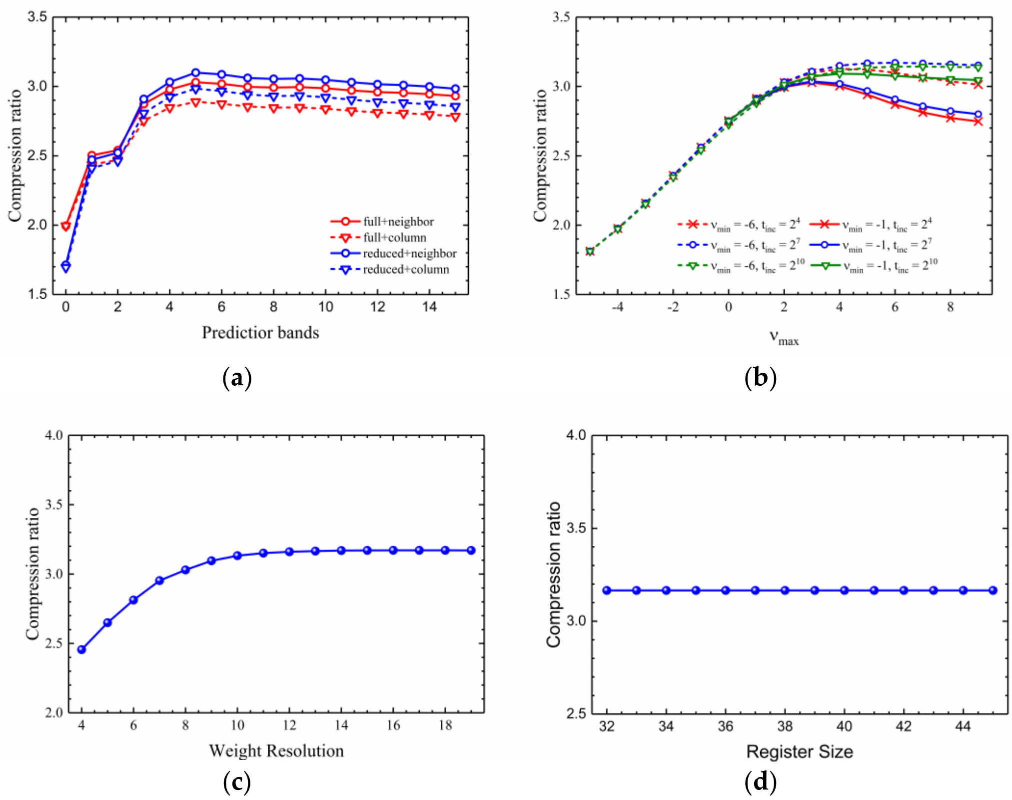

Figure 9. Compression ratio for different predictor parameters: (**a**) number of prediction bands, compression mode, and local sum type; (**b**) weight update scaling exponent final value, weight update scaling exponent initial value, and weight update scaling exponent change interval; (**c**) weight resolution; (**d**) register size.

4.2.2. Weight Adaption Parameters

Figure 9b shows the compression ratio as a function of the weight update scaling exponent final parameter, ν_{max}, for several different combinations of the weight update scaling exponent initial parameter, ν_{min}, and the weight update scaling exponent change interval, t_{inc}. It can be seen that the values of ν_{min} and t_{inc} have little influence on the overall performance compared with the value of ν_{max}. In accordance with the regulations stipulated in the standard, the weight update scaling exponent, $\rho(t)$, increases by increments of one until the final value of $\nu_{max} + D - \Omega$, where D is the bit depth of the image acquired by the CCD detector, and Ω is the weight resolution parameter. A smaller value of $\rho(t)$ yields larger weight increments, resulting in faster adaption to data statistics but worse steady-state compression performance. Therefore, we can see that, when the initial value of ν_{max} is small, the adaptation speed of the image statistics is fast, but the stability of the compression effect is poor, resulting in a lower compression ratio. Then, the compression ratio tends to improve as ν_{max} increases; when the value of ν_{max} increases to a certain point, there will be a compromise between the adaptation speed of the image statistics and the stability of the compression effect, resulting in an optimal compression ratio being achievable. As the value of ν_{max} continues to increase, the compression ratio even experiences a slight decrease. The results presented below show that the case of $\nu_{max} = 6$, $\nu_{min} = -6$ and $t_{inc} = 2^7$ provides the optimal performance.

4.2.3. Weight Resolution

Figure 9c shows the compression ratio as a function of the weight resolution parameter, Ω. The compression performance suffers significantly when the value of Ω is close to the minimum allowed value. Increasing the value of Ω means that more bits are used to represent the weight component; thus, the prediction is more accurate, which results in improved compression effectiveness and higher implementation complexity. However, the weight increment will always be a multiple of two when $\Omega \geq \nu_{max} + D + 2$ according to the definition of the next weight vector defined in the standard [23]. Essentially, the weight value's least significant bit remains unchanged with each update, which means that the available weight resolution is not being fully utilized. As a result, the compression ratio curve tends to flatten beyond a certain point. Simultaneously, a larger value of Ω implies a need to use a greater number of bits for encoding. As indicated by the results of this experiment, $\Omega = 13$ produced a good compromise.

4.2.4. Register Size

The results shown in Figure 9d suggest that the value of the register size, R, has almost no impact on the compression effectiveness, which means that the overflow may be so rare that there are few occasions when a large value of R is needed to prevent overflow. The compression will still be lossless, even when an overflow occurs. Consequently, a large value of R is not required because it is unlikely to improve compression and will also increase the implementation complexity. Therefore, the value of R can be set to the minimum value allowed by the standard, which is 32.

4.3. Entropy Coder Settings

4.3.1. Sample-Adaptive Entropy Coders

- Initialization and adaptation parameter

Figure 10a shows the compression ratio as a function of γ^* for several combinations of the initial count exponent, γ_0, and the accumulator initialization table, $\{k'_z\}_{z=0}^{N_z-1}$, which is simplified as an accumulator initialization constant, K; i.e., $k'_z = K$ for all bands. The interval at which the accumulator and counter of this encoding approach are rescaled is controlled by the rescaling counter size parameter, γ^*. A smaller value of γ^* is shown to yield a faster adaptation and better compression performance, and it generally makes the compression effectiveness less sensitive to the values of γ_0 and K. When γ_0 is a small value, the compression performance is less sensitive to the value of K. The value of γ_0 has almost no impact on the compression performance by avoiding the minimum allowed value of K.

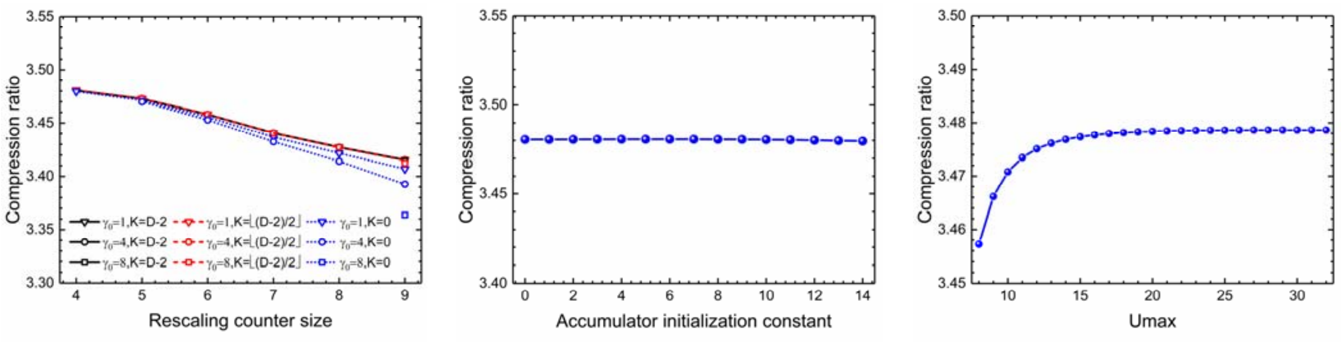

(**a**) (**b**) (**c**)

Figure 10. Compression ratio for different sample-adaptive entropy coder parameters: (**a**) rescaling counter size parameter, γ^*; initial count exponent, γ_0; (**b**) accumulator initialization constant, K; (**c**) unary length limit parameter, U_{max}.

Figure 10b shows the compression ratio as a function of K obtained via the combination of $\gamma^* = 4$ and $\gamma_0 = 1$. The curve is remarkably flat, which means that the value of K has almost no effect on the compression performance.

- Unary length limit

The compression ratio as a function of the unary length limit parameter, U_{max}, is presented in Figure 10c, which shows that increasing the value of U_{max} yields a dramatic improvement in the compression ratio when U_{max} is close to the minimum allowed value. When the value of U_{max}, which limits the length of the unary code part, is set too small, it results in notably poor coding efficiency for the mapped prediction residual, with relatively smaller magnitudes. However, the cost of hardware implementation will remove this benefit to the compression effectiveness when the value of U_{max} is sufficiently large. Based on the results displayed in Figure 10, $U_{max} \approx 18$ appears to offer a reasonable compromise between the hardware implementation complexity and compression performance.

4.3.2. Block-Adaptive Entropy Coder

- Sample encoding order

The compression ratio under block-adaptive entropy coding when the BSQ, BIL, and BIP encoding orders are used along with the sample-adaptive compression performance are presented in Figure 11a. The value of the block size used in this experiment is 16. The BSQ appears to perform slightly better than the BIL, and the BIP encoding order typically performs much more poorly than the other two. The BIP encoding order mixes samples from different bands within the same block. Therefore, the similarity of the data within a block is not as high as that of the first two encoding methods. Furthermore, when the width of an image is a multiple of the block size, J, the blocks generated by the BIL and BSQ encoding orders are the same, but the ordering of these blocks within the image is different. Compared with the BIL encoding order, the BSQ encoding order makes it easier for zero blocks to be adjacent, resulting in a slightly higher compression ratio. In general, sample-adaptive coding presents better performance than the block-adaptive approach by a considerable degree. The advantages of block-adaptive entropy coding can only be observed when there is a significant presence of zero blocks within the mapped prediction residuals.

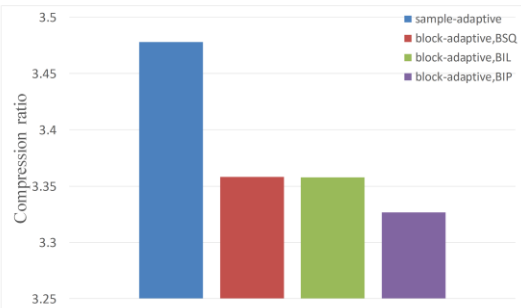

(**a**)

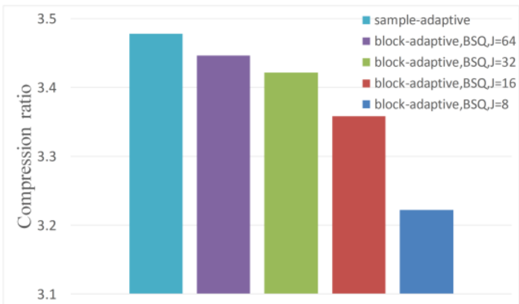

(**b**)

Figure 11. Compression ratio for different parameters of the block-adaptive entropy coder along with the results of the sample-adaptive approach: (**a**) sample encoding order; (**b**) block size, J, when a BSQ encoding order is used.

- Block size

Figure 11b shows the compression ratio under block-adaptive entropy coding using the BSQ encoding order when the value of the block size, J, is 8, 16, 32, or 64, along with the results of the sample-adaptive approach. The figure suggests that using a larger block size results in a higher compression ratio. This is because, although the value of the block size, J, is small, it allows the entropy encoder to adapt faster to changes in the data source statistics and possibly obtain an increase in the compression ratio; however, since block-adaptive entropy coding specifies the encoding method for each block by using additional bits, when the block size is small, due to the additional bits, the bit cost increases much more than the positive impact it brings, thus producing a result where a small block size leads to a low compression ratio.

4.4. Summary

The experimental results presented above indicate that the rearrange method introduced in this paper provides considerable advantages over the natural and traditional approaches. Moreover, the sample-adaptive encoder outperforms the block-adaptive encoder in terms of compression performance. Nevertheless, the predictor parameters appear to have much more impact on the compression effectiveness than the entropy coder parameters, particularly for the prediction mode, local sum type, number of prediction bands, and weight adaptation parameters. On the basis of these results, the adequate compression settings of the CCSDS-123 for the rearranged LASIS data are listed in Table 1.

Table 1. Adequate compression settings of the proposed compression scheme.

	Name	Symbol	Setting
Predictor parameters	Prediction mode		Reduced mode
	Local sum type		Neighbor-oriented
	Number of prediction bands	P	5
	Weight update scaling exponent initial parameter	v_{min}	-6
	Weight update scaling exponent final parameter	v_{max}	6
	Weight update scaling exponent change interval	t_{inc}	2^7
	Weight component resolution	Ω	13
	Register size	R	32
Entropy coder parameters (sample-adaptive)	Initial count exponent	γ_0	1
	Rescaling counter size	γ^*	4
	Accumulator initialization constant	K	4
	Unary length limit	U_{max}	18

5. Conclusions

The LASIS instrument encounters unprecedented problems in the hyperspectral image compression approach because of its unique data characteristics. This paper briefly outlined the imaging principle and the characteristics of data acquired by the LASIS. A new lossless compression technique for the LASIS has been proposed, which combines a novel data rearrange method with the CCSDS-123. The interference information superimposed on one frame image of the acquired data can be separated with the proposed rearrange approach, and then, the CCSDS-123 standard is employed to process the rearranged data cube. Several experiments were conducted on 30 hyperspectral images for different scenes acquired by the LASIS instrument to examine the performance of the proposed compression scheme. The experimental results indicate that the average compression ratio of the proposed compression method is approximately 32.9% higher than that obtained by combining the traditional rearrange approach with the standard. In addition, an adequate optimal combination of the compression parameters has been presented, and it yields a 19.6% improvement over the default settings. These results can provide instructive information for the lossless compression of other hyperspectral interferometers based on a LASIS-like principle.

Author Contributions: Conceptualization, L.Y. and H.L.; methodology, L.Y.; investigation, L.Y.; writing—original draft preparation, L.Y.; writing—review and editing, W.L. and J.L.; funding acquisition, L.Y. All authors have read and agreed to the published version of the manuscript.

Funding: This research was funded by the Scientific Research Program of Shaanxi Provincial Education Department (Grant No. 21JK0787), the Natural Science Foundation of Shaanxi Province (Grant No. 2020JQ-651), and the Ph.D. Stand-Up Fund of Xi'an University of Technology (Grant No. 108-451122002).

Institutional Review Board Statement: Not applicable.

Informed Consent Statement: Not applicable.

Data Availability Statement: Not applicable.

Conflicts of Interest: The authors declare no conflict of interest.

References

1. Chen, X.; Lv, Q.; Tang, Y.; Wang, J.; Zhao, N.; Tan, Z.; Li, W.; Liu, Y.; Si, J.; Xiangli, B. Investigating the Influence of the Diffraction Effect on Fourier Transform Spectroscopy with Bandpass Sampling. *Appl. Sci.* **2022**, *12*, 10068. [CrossRef]
2. Rousset-Rouviere, L.; Coudrain, C.; Fabre, S.; Poutier, L.; Loke, T.; Fridman, A.; Blaaberg, S.; Baarstard, I.; Skauli, T.; Mocoeur, I. SYSIPHE system: A state of the art airborne hyperspectral imaging system. Initial results from the first airborne campaign. *Proc. SPIE* **2014**, *9249*, 92490W.
3. Zhang, X.; Zhu, J.; Huang, L.; Zhang, Y.; Wang, H.; Deng, J.; Guo, F. Luminous Flux Utilization of Static Birefringent Fourier Transform Imaging Spectrometer with Zoomable Spectral Resolution. *Appl. Sci.* **2023**, *13*, 5132. [CrossRef]
4. Zhang, G.; Wang, S.; Li, L.; Hu, X.; Hu, B. Interference data correction methods for lunar observation with a large-aperture static imaging spectrometer. *Appl. Opt.* **2016**, *55*, 8770–8778. [CrossRef] [PubMed]
5. Su, L.; Yuan, Y.; Xiangli, B.; Huang, F.; Cao, J.; Li, L.; Zhou, S. Spectrum Reconstruction Method for Airborne Temporally-Spatially Modulated Fourier Transform Imaging Spectrometers. *IEEE Trans. Geosci. Remote* **2014**, *52*, 3720–3728. [CrossRef]
6. Barducci, A.; Castagnoli, F.; Castellini, G.; Guzzi, D.; Lastri, C.; Marcoionni, P.; Nardino, V.; Pippi, I. Developing a new hyperspectral imaging interferometer for earth observation. *Opt. Eng.* **2012**, *51*, 111706. [CrossRef]
7. Lucey, P.G.; Wood, M.; Crites, S.T.; Akagi, J. A LWIR hyperspectral imager using a Sagnac interferometer and cooled HgCdTe detector array. *Proc. SPIE* **2012**, *8390*, 83900Q.
8. Xiangli, B.; Lv, Q.; Cai, Q. Fourier transform imaging spectroscopy. *Sci. Sin. Inform.* **2020**, *50*, 1462–1474.
9. Cai, Q.; Xiangli, B.; Huang, M.; Han, W.; Pei, L.; Bu, M. Prototype development and field measurements of high etendue spatial heterodyne imaging spectrometer. *Opt. Commun.* **2018**, *410*, 403–409. [CrossRef]
10. Zhang, W.-L.; Liu, Z.-Y.; Wang, H.; Chen, Y.; Wang, Y.; Zhao, Z.-Z.; Sun, T. Research status of spatial Heterodyne spectroscopy–A review. *Microchem. J.* **2021**, *166*, 106228. [CrossRef]
11. Hernandez-Cabronero, M.; Kiely, A.B.; Klimesh, M.; Blanes, I.; Ligo, J.; Magli, E.; Serra-Sagrista, J. The CCSDS 123.0-B-2 "Low-Complexity Lossless and Near-Lossless Multispectral and Hyperspectral Image Compression" Standard: A comprehensive review. *IEEE Geosci. Remote Sens. Mag.* **2021**, *9*, 102–119. [CrossRef]
12. Blanes, I.; Kiely, A.; Hernández-Cabronero, M.; Serra-Sagristà, J. Performance Impact of Parameter Tuning on the CCSDS-123.0-B-2 Low-Complexity Lossless and Near-Lossless Multispectral and Hyperspectral Image Compression Standard. *Remote Sens.* **2019**, *11*, 1390. [CrossRef]
13. Dua, Y.; Kumar, V.; Singh, R.S. Comprehensive review of hyperspectral image compression algorithms. *Opt. Eng.* **2020**, *59*, 090902. [CrossRef]
14. Melian, J.; Diaz, M.; Morales, A.; Guerra, R.; Lopez, S.; Lopez, J.F. A Novel Data Reutilization Strategy for Real-Time Hyperspectral Image Compression. *IEEE Geosci. Remote Sens.* **2022**, *19*, 1–5. [CrossRef]
15. Li, R.; Pan, Z.; Wang, Y.; Wang, P. The correlation-based Tucker decomposition for hyperspectral image compression. *Neurocomputing.* **2021**, *419*, 357–370. [CrossRef]
16. Zheng, T.; Dai, Y.; Xue, C.; Zhou, L. Recursive Least Squares for Near-Lossless Hyperspectral Data Compression. *Appl. Sci.* **2022**, *12*, 7172. [CrossRef]
17. Deng, J.; Wu, C.; Chen, J. Multi-Spectral Image Compression Based on Rate-Distroiton Slope Lifting. *Acta Opt. Sin.* **2004**, *24*, 299–303.
18. Xiao, J.; Zhou, Y.; Wu, C.; Yang, J.; Xiang, L. The Image Compression Technology of the Large Aperture Static Imaging Interference Spectrometry. *Acta Opt. Sin.* **2004**, *24*, 1494–1498.
19. Ma, J.; Wu, C.; Chen, D.; Guo, J. Interference Multispectral Image Compression with Adaptive Distortion Control in Fourier Domain. In Proceedings of the Conference Record of 2007 Data Compression Conference, Snowbird, UT, USA, 27–29 March 2007; p. 395.
20. Wang, K.Y.; Wu, C.K.; Kong, F.Q.; Zhang, L. An improved partial SPIHT with classified weighted rate-distortion optimization for interferential multispectral image compression. *Chin. Opt. Lett.* **2008**, *6*, 331–333. [CrossRef]
21. Li, Y.; Ma, J.; Wu, C. Three-Dimensional Orientation Prediction-Based Wavelet Transform for Interference Multi-Spectral Images Compression. *Acta Opt. Sin.* **2008**, *28*, 2281–2287.
22. Wen, J.; Ma, C.; Zhao, J. FIVQ algorithm for interference hyper-spectral image compression. *Opt. Commun.* **2014**, *322*, 97–104. [CrossRef]
23. Consultative Committee for Space Data Systems. Lossless Multispectral & Hyperspectral Image Compression CCSDS 123.0-B-1. 2012. Available online: https://public.ccsds.org/Pubs/123x0b1ec1s.pdf (accessed on 30 May 2014).

24. Auge, E.; Sanchez, J.E.; Kiely, A.; Blanes, I.; Serra-Sagrista, J. Performance impact of parameter tuning on the CCSDS-123 lossless multi- and hyperspectral image compression standard. *J. Appl. Remote Sens.* **2013**, *7*, 074594. [CrossRef]
25. Consultative Committee for Space Data Systems. Lossless Multispectral & Hyperspectral Image Compression CCSDS 120.2-G-1. 2015. Available online: https://public.ccsds.org/Pubs/120x2g1s.pdf (accessed on 10 December 2016).